International Journal of Nanomedicine

Dovepress
Taylor & Francis Group

Open Access Full Text Article

ORIGINAL RESEARCH

Macrophage Membrane-Coated Liposomes Delivering Vonoprazan Disrupt Mitochondrial Oxidative Phosphorylation in Diffuse Large B-Cell Lymphoma

Weiwei Wang[1,*], Lei Wang[2,*], Qingqing Fan[3,*], Jingyan Xu[1], Yifan Li[4], Jiale Xu[4], Bei Zhao[2], Dan Ge[2], Longying Xiong[2], Yanping Wu[2], Yun Zhu[4,5], Min Chen[4]

[1]Department of Hematology, Nanjing Drum Tower Hospital Clinical College of Nanjing University of Chinese Medicine, Nanjing, Jiangsu Province, 21008, People's Republic of China; [2]Department of Gastroenterology, Nanjing Drum Tower Hospital, The Affiliated Hospital of Nanjing University Medical School, Nanjing, Jiangsu Province, 210008, People's Republic of China; [3]Department of Pharmacy, West China Hospital, Sichuan University, Chengdu, 610041, People's Republic of China; [4]Department of Gastroenterology, Nanjing Drum Tower Hospital Clinical College of Nanjing University of Chinese Medicine, Nanjing, Jiangsu Province, 21008, People's Republic of China; [5]Department of Pharmacy, Nanjing Drum Tower Hospital, The Affiliated Hospital of Nanjing University Medical School, Nanjing, 210008, People's Republic of China

*These authors contributed equally to this work

Correspondence: Yun Zhu; Min Chen, Email njglyyzhuy@cpu.edu.cn; croweminchan@nju.edu.cn

---

Background: A significant proportion of patients fail to respond adequately to the standard R-CHOP regimen for diffuse large B-cell lymphoma (DLBCL). Rapid proliferation requires energy and the interaction between H^+ ions and mitochondria suggests that regulating acid secretion in tumor cells may be a therapeutic strategy for DLBCL. This study constructed a macrophage membrane-coated liposomal formulation (MM-Lipid@Vpz) for the targeted delivery of vonoprazan to combat DLBCL, which enables the evasion of the reticuloendothelial system, ensuring enhanced specificity in tumor targeting.

Methods: The vonoprazan was delivered by encapsulating liposomes with pre-isolated macrophage membranes, targeted to DLBCL cells and evaluated for changes in cell function. The cellular transcriptome was collected to analyze the mechanism of drug action. An in vivo DLBCL nude mouse subcutaneous tumor model was also established to validate in vitro drug efficacy. In addition, MM-Lipid @Vpz was combined with doxorubicin (Dox) in this study to investigate the effect of action between the two.

Results: Lipid@Vpz was prepared by mixing lecithin, cholesterol, DSPE-PEG$_{2000}$ and vonoprazan at a mass ratio of 100:30:1:10 and dissolving them in anhydrous ethanol. After fusing the macrophage membrane with Lipid@Vpz by extrusion, the particle size increased to 135.37 ± 12.55 nm and the zeta potential changed to −20.42 ± 1.37 mV. Compared with Lipid@Vpz, MM-Lipid@Vpz significantly increased the intracellular internalization efficiency of vonoprazan by 4.42 times and increased the tumor accumulation in mice by 60.10%. In addition, MM-Lipid@Vpz induced apoptosis in SU-DHL-8 cells at a rate 1.26 times that of Lipid@Vpz and increased the intracellular reactive oxygen species (ROS) level to 1.18 times that of Lipid@Vpz by disrupting mitochondrial oxidative phosphorylation (OXPHOS) and altering mitochondrial morphology. When combined with existing first-line agents such as Dox, MM-Lipid@Vpz manifested synergistic antitumor effects, further augmenting tumor suppression and potentially mitigating drug resistance.

Conclusion: Bionic macrophage membrane-encapsulated vonoprazan preparations inhibit DLBCL cellular energy metabolism both in vivo and ex vivo by affecting mitochondrial OXPHOS, which provides data to support the improvement of the prognosis of patients with DLBCL by precise metabolic disruption.

Keywords: DLBCL, vonoprazan, macrophage membranes, doxorubicin, oxidative phosphorylation

---

Introduction

DLBCL represents a highly aggressive and heterogeneous malignancy.[1] Despite the efficacy of the standard R-CHOP regimen, a significant proportion (30–40%) of patients experience disease progression or relapse post-treatment.[2]

Received: 4 February 2025
Accepted: 18 June 2025
Published: 24 June 2025

Immunotargeted therapy, small molecule inhibitors, and epigenetic regulation are emerging treatment strategies for DLBCL, but these therapies all have high levels of toxicity and drug resistance.[3] The clinical challenge posed by DLBCL underscores the importance of exploring novel therapeutic avenues that can improve patient outcomes.[4] Cellular energy metabolism emerges as a critical factor influencing both the efficacy of current therapeutic strategies and the progression of the disease. As a rapidly proliferating malignancy, DLBCL cells require substantial energy resources to support their growth and invasive behavior.[5,6] Research has revealed that alterations in cellular energy metabolism can contribute to drug resistance,[7–10] thereby highlighting the potential of metabolic inhibitors as a promising therapeutic target for DLBCL.[11]

A key aspect of tumor cell metabolism is its adaptation to an acidic microenvironment characterized by elevated H^+ ion concentrations.[12,13] This metabolic reprogramming not only meets the heightened energy demands of tumor cells but also drives changes in the tumor transcriptome, potentially impacting tumor biology and response to therapy.[14] Within this framework, the interplay between H^+ ions, ATP homeostasis, and the electron transport chains (ETCs) within mitochondria becomes particularly relevant.[15–17] Mitochondria, as central hubs of cellular energy production, maintain ATP synthesis through the ETCs by establishing a transmembrane proton gradient.[18] Given the pivotal role of mitochondria in energy metabolism, interventions targeting mitochondrial function present a viable strategy for enhancing treatment efficacy in DLBCL.

The pH dynamics within the gastric environment, influenced by H^+ concentration, play a significant role in modulating mitochondrial energy metabolism in gastric-associated lymphomas.[19] This observation suggests that manipulating the pH could have implications for DLBCL therapy. Potassium-competitive acid blockers (P-CABs), a class of drugs designed to inhibit proton pumps, offer a rapid onset of action, prolonged duration of effect, and improved stability compared to traditional acid-suppressing agents.[20,21] Clinical evidence supports the notion that combining acid suppressant with first-line lymphoma treatments may enhance progression-free survival (PFS) rates.[22] By altering the balance of H^+ and ATP, P-CABs such as vonoprazan might indirectly affect mitochondrial ATP homeostasis and energy metabolism, thereby presenting a potential avenue for optimizing metabolic therapy in DLBCL. Specifically, vonoprazan's ability to inhibit proton pumps leads to changes in intracellular pH levels. In non-gastric cells, these changes can influence the mitochondrial transmembrane potential and subsequently disrupt the ETCs, which is crucial for OXPHOS. Multiple studies have indicated that vonoprazan exhibits good safety profiles in various organs or cell types.[23,24] A further study confirmed that vonoprazan has a high plasma binding rate,[25] and its low concentration limits its direct metabolic interactions in non-gastric cells, resulting in minimal impact on OXPHOS under normal conditions. However, in the context of tumor cells, where there is already an altered metabolic state and increased reliance on mitochondrial function for energy production, this subtle disruption can significantly impair OXPHOS efficiency. This makes targeting the metabolic vulnerabilities of DLBCL through the delivery of P-CABs like vonoprazan via drug delivery systems an appealing strategy for overcoming resistance and improving therapeutic outcomes.

Drug delivery systems based on mitochondrial membranes, designed by mimicking their composition and function to create carriers, utilize membrane potential, proteins, or lipid components to achieve targeted drug delivery and release.[26] Most drug delivery systems are easily recognized and phagocytosed by macrophages in organs such as the liver and spleen due to their surface charge or particle size characteristics, leading to drug clearance or accumulation in non-target tissues.[27] Macrophages, as intrinsic immune cells,[28,29] possess unique properties that exhibit high affinity to tumor cells and also evade clearance by the reticuloendothelial system, making them ideal for enhancing drug delivery specificity.[30–32] Studies have demonstrated that coating with macrophage membranes containing intact membrane proteins preserves the macrophage receptors and the "self-marker" CD47 used for cell interactions, which hinders their recognition by immune cells.[33] Our study introduces liposomes coating with macrophage membranes to deliver vonoprazan (MM-Lipid @Vpz) directly to tumor sites. We assessed the affinity of MM-Lipid@Vpz for DLBCL cells to determine their selective binding and internalization, aiming to enhance therapeutic outcomes while minimizing off-target effects. Additionally, the impact of MM-Lipid@Vpz on mitochondrial function, focusing on OXPHOS and ATP synthesis, critical for tumor cell survival was evaluated. Transcriptome sequencing was also conducted to identify affected molecular targets and pathways, offering insights into pharmacological mechanisms and potential biomarkers for therapeutic response. In summary, this study proposes a novel DLBCL therapy strategy, leveraging macrophage membrane vesicles for targeted

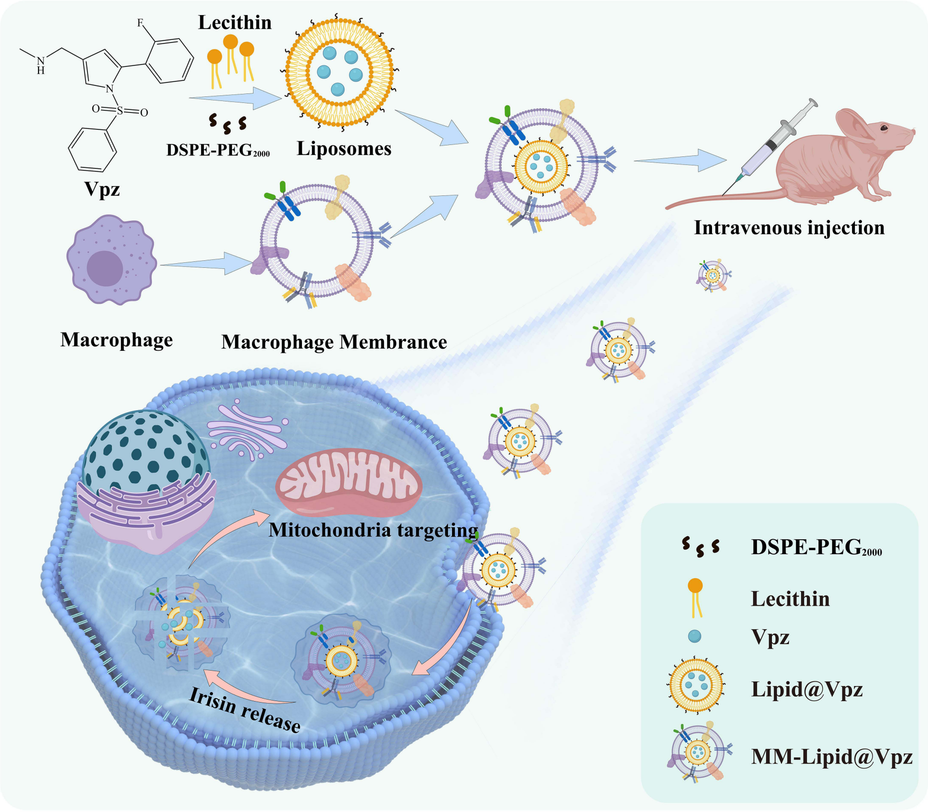

Scheme 1 Schematic representation of the synthesis and anti-tumor mechanism of MM-Lipid@Vpz.

drug delivery and mitochondrial modulation, integrating findings from affinity studies, mitochondrial assays, and transcriptome analysis to uncover the therapeutic potential of MM-Lipid@Vpz (Scheme 1).

Materials and Experimental Procedures

Cell Lines

Human lymphoma cell line SU-DHL-8, and mouse RAW264.7 macrophages were purchased from ATCC and cultured at 37°C and 5% CO_2 in RPMI-1640 and DMEM medium containing 10% Fetal Bovine Serum (FBS) and 1% penicillin/streptomycin, respectively.

Reagents and Animals

Egg yolk lecithin was purchased from Avital (Shanghai, China). IR780 and coumarin 6 (C6) was purchased from Aladdin Reagent Database Inc. (Shanghai, China). Vonoprazan was purchased from MCE (Shanghai, China). Ruixi Biologicals Co.Ltd (Xi'an, China) provided DSPE-PEG$_{2000}$. Coomassie Blue staining solution was purchased from Beyotime (Shanghai, China) Male 5-week-old Balb/c-nude mice were purchased from Nanjing Annuokang Biotechnology Co., Ltd. These mice adapted to the environment for 1 week before the experiment. This animal research was approved by the Experimental Animal Management Ethics Committee of Nanjing Drum Tower Hospital (2025AE01023). All animal experiments were conducted in accordance with the ARRIVE guidelines and the National Institutes of Health Guidelines for the Care and Use of Laboratory Animals.

Bionic Membrane Preparation

Mix lecithin, cholesterol, DSPE-PEG$_{2000}$, and vonoprazan in a ratio of 100:30:1:10 and dissolve them in anhydrous ethanol. And the lipid mixture was continuously and homogeneously injected into phosphate buffered saline (PBS) under magnetic stirring at 1000 rpm for 10 min, and free vonoprazan and Lipid@Vpz were separated using ultrafiltration tubes (50 KDa, Millipore).

Cell membranes were isolated from RAW264.7 cells using the Membrane Protein Extraction Kit (abbkine, Wuhan, China). The protein content of purified cell membranes was determined using the BCA protein assay and MM-Lipid @Vpz was obtained by sequentially extruding the membranes through polycarbonate membranes with pore sizes of 400 and 200 nm after mixing the membranes in a liposome solution at a protein-lipid ratio of 1:10.

Bionic Membrane Characterization

Their particle size distribution and zeta potential were measured by Zetasizer Nano (Malvern Instruments, Malvern) using dynamic light scattering (DLS) and electrophoretic light scattering (ELS) respectively. The morphology of the particles was observed by electron transmission microscopy. Using UV-Vis spectrophotometry to determine the drug loading (DL) and encapsulation efficiency (EE) of the tested drug. The calculated formula of EE as follows:

$$EE\% = \frac{vonoprazan\ encapsulated}{Total\ vonoprazan} \times 100\%$$

$$DL\% = \frac{vonoprazan\ encapsulated}{quality\ of\ thecarrier} \times 100\%$$

The following is the Korsmeyer-Peppas model, where Q is the cumulative percentage of drug release at a given time (t), k is the diffusion constant, and n is the release exponent.[34]

$$Q = k \times t^n$$

In vitro Drug Release

Vpz, Lipid@Vpz and MM-Lipid@Vpz were placed in dialysis bags of molecular weight 3500 Da and immersed in 50 mL of PBS buffer with a pH of 7.4 containing 5.0% Tween and shaken at 50 rpm at 37°C, respectively. The drug content of the released PBS buffer was quantified at different times. The experiments were repeated three times.

Hemolysis

Collect whole blood from healthy mouse eyes and collect blood cells. Take 1 mL of material solution (25–100 µg/mL), 1 mL of ultrapure water, and 1 mL of PBS, and mix with 20 µL of blood cells. Incubate at 37°C for 4 hours and record the hemolysis situation. After centrifugation, measure the absorbance of the sample supernatant at 542 nm using a microplate reader.

Stability Testing

Place MM-Lipid@Vpz in a 4°C environment and record its particle size and encapsulation efficiency at various time points (0, 6, 12, 24, 48, and 72 h) within 72 hours, while also paying attention to its appearance changes. Additionally, place freshly prepared MM-Lipid@Vpz in PBS containing 10% FBS, then let it stand at 37°C for 24 hours, and sample to measure its particle size changes.

Cellular Uptake

Using coumarin C6 as a fluorescent probe, dissolved in ethanol, and loaded into the two formulations mentioned above. The concentration of C6 in the final preparation was quantified to be 10 µg/mL using a SparkTM 10 M multimode microplate reader (Tecan Group Ltd., Männedorf, Switzerland).

FREE-C6, Lipid@C6 and MM-Lipid@C6 were co-incubated with SU-DHL-8 cells and RAW264.7 cells for 3, 6, and 9 min, respectively, and the cells were collected and the nuclei were stained with DAPI for 5 min, and the fluorescence intensity was recorded by flow cytometry and confocal microscopy, respectively.

In vivo Imaging

Nine mice were randomly divided into three groups with equal numbers. The observers who recorded the data were unaware of the group assignments. IR780 is used for labeling Lipid and MM-Lipid. The method is the same as the marking of C6 mentioned above. The concentration is quantified as 20 μg/mL. FREE-IR780, Lipid@IR780 and MM-Lipid@IR780 were injected into mice via tail vein. Induction of anesthesia with isoflurane. Fluorescein distribution was imaged at 6,12,24 h post-injection using a small animal in vivo imager (IVIS Spectrum, Perkin Elmer, USA). And the fluorescence signals of mouse heart, liver, spleen, lung and kidney were recorded.

Cell Counting Kit-8 (CCK8)

Cells were seeded in a 96-well plate at a density of 5×10^3cells per well. After drug treatment, CCK-8 solution was added and incubation continued until the absorbance value of the control well reached 1. The optical density values were then measured at 450 nm using a microplate reader.

Western Blot

The protein concentration was quantified using BCA, and the samples were boiled. Equal amounts of the samples were then subjected to SDS-PAGE electrophoresis and transferred onto a PVDF membrane. The primary antibody was incubated with the membrane overnight at 4°C. The following day, after incubation with the secondary antibody, the membrane was exposed for visualization.

To verify the integrity of the membrane protein, incubate the gel with about 20–30mL of Coomassie Blue staining solution for 30 minutes after SDS-PAGE electrophoresis. Then, remove the staining solution, rinse the gel with deionized water, and take a photograph.

The antibodies were detected by immunoblotting as follows:CCR2 (MCE, HY-P80385); E-Cadherin (Abcam, ab314063); Tublin (Selleck, F0167); Bcl-2 (ABclonal, A20777); Caspase3 (Selleck, F1080); Cleaved-Caspase3 (Selleck, F0135); MT-ND5 (HUABIO, #ER1913-30); MT-ATP6 (HUABIO, #ER60496); MT-CYB (ABclonal, A9762); MT-CO3 (Abcam, ab110259).

Apoptosis, ROS and MMP Assay by Flow Cytometry in vitro

Cells were inoculated into 6-well plates at a density of 5×10^5 cells/well, processed single-cell suspension was collected. Apoptosis was observed by Membrane Associated Protein V-FITC/PI Apoptosis Detection Kit (Yisheng Biotechnology Co., LTD, Shanghai, China), reactive oxygen species (ROS) levels in cells were detected by fluorescent probe DCFH-DA (Yisheng Biotechnology Co., LTD, Shanghai, China), and changes in mitochondrial membrane potential (MMP) levels were detected by JC-1 Membrane Potential Detection Kit (Yisheng Biotechnology Co., LTD, Shanghai, China), and fluorescence intensities were all observed by flow cytometry.

Determination of ATP and NAD^+/NADH Levels

ATP concentrations and NAD^+/NADH ratios were quantified using an ATP assay kit and a NAD^+/NADH assay kit (Beyotime, Shanghai, China).

Seahorse XF 24 Metabolic Flux Analysis

Oxygen consumption rate (OCR) was measured by the Seahorse XF bioenergetics assay using an Agilent Seahorse XF 24 analyzer and a cellular mitochondrial stress test kit (Agilent Technology, USA).[35] Briefly, drug-treated SU-DHL-8 cells were transferred to buffer-free medium and incubated at 37 °C in a CO2-free incubator for 45 min. Oligomycin (2.5 μM), carbonyl cyanide-4-(trifluoromethoxy) phenylhydrazone (FCCP, 2 μM), rotenone, and antimycin A (0.5 μM) were sequentially added to the probe plate dosing wells. The OCR was then calculated automatically by a Seahorse XF 24 analyzer.

Sequencing

SU-DHL-8 cells were collected and rapidly frozen, and transcriptome sequencing was performed by Majorbio Co. Ltd. (Shanghai, China) Three independent replicates per sample.

Establishment of Mouse Subcutaneous Tumor Model and Drug Treatment and Evaluation

Twenty mice were randomly divided into four groups with equal numbers and 4×10^6 cells were implanted into the left axilla of each mouse and tail vein drug treatment was given every two days when the mean tumor size reached $50mm^3$ and body weights and tumor lengths and widths were recorded.[36] The pre-experiment was based on the IC_{50} of MM-Lipid@VPZ to design the concentration gradient, combined with the literature dosage of doxorubicin, and after comprehensive consideration, Vpz, Lipid@Vpz, MM-Lipid@Vpz, and Dox were administered at doses of 5 mg/kg, 5 mg/kg, 5 mg/kg, and 1 mg/kg, respectively. The person administering the medication and the observer recording the data are unaware of the group assignments. At the end of treatment, nude mice were euthanized under anesthesia and tumors, heart, liver, spleen, lungs and kidneys were stripped and fixed in tissue fixative containing 4% paraformaldehyde for 24 h. Tumor and organ tissues were collected from the nude mice and stained with Hematoxylin and Eosin (HE) to observe any histopathological changes. Blood was collected from nude mice for hematological and biochemical analyses. White blood cells (WBC), platelets (PLT), red blood cells (RBC), alanine aminotransferase (ALT), aspartate aminotransferase (AST), creatinine (CREA), and blood urea nitrogen (BUN) were recorded to observe in vivo hematology and toxicity to organs.

Terminal Deoxynucleotidyl Transferase DUTP Nick Labeling (TUNEL), Ki-67 and ROS Assays

Paraffin-embedded tissue samples were deparaffinized and stained for TUNEL, Ki67 and ROS according to standard protocols and nuclei were stained with DAPI.

Mouse Bone Marrow-Derived Macrophages (BMDM) Extraction

Soak the separated hind legs of mice in ethanol and rinse. Cut open the bone in 10% DMEM medium and rinse the bone marrow with a syringe. Collect cell suspension and treat with red blood cell lysis buffer. Resuspend and inoculate with medium containing M-CSF. On the third day, add stimulating factors to the culture medium. Obtain macrophages one week later.

Statistical Analysis

Experimental procedures were repeated at least three times, and the data were presented as mean ± SD. Student's t-test was used for comparisons between two groups and One-way analysis of variance (ANOVA) was used for multiple comparisons by GraphPad Prism 8 (GraphPad Software, San Diego, CA, USA). Statistical significance was set at $^{*}P < 0.05$, $^{**}P < 0.01$, $^{***}P < 0.001$ and $^{****}P < 0.0001$.

Results and Discussion

Preparation Characterization and Evaluation of MM-Lipid@Vpz for Macrophage Targeting

In order to deliver vonoprazan specifically to the tumor site for therapeutic efficacy, a strategy was developed using the immune recognition function of macrophages in order to deliver vonoprazan specifically to the tumor site, where conventional delivery methods bring about a high concentration of vonoprazan in the acidic tubules of gastric lining cells.[37] Involving delivery of vonoprazan encapsulated in liposomes modified with isolated macrophage membranes. Transmission electron microscopy (TEM) analysis confirmed the integrity structure, and a clear core-shell structure could be observed at MM-Lipid@Vpz (Figure 1A). The particle size of MM-Lipid@Vpz increased from 86.46 ± 26.79 nm to 135.37 ± 12.55 nm as compared to uncoated Lipid@Vpz, which was attributed to the thickness of the macrophage membrane[38] and maintaining polydispersity coefficients (PDI) within an appropriate range (Figure 1B). Additionally, surface charge conveyed a zeta potential of −10.77 ± 0.95 mV for Lipid@Vpz, in contrast to the various phospholipids and proteins present in the macrophage membrane which resulted in a more negative zeta potential for MM-Lipid@Vpz

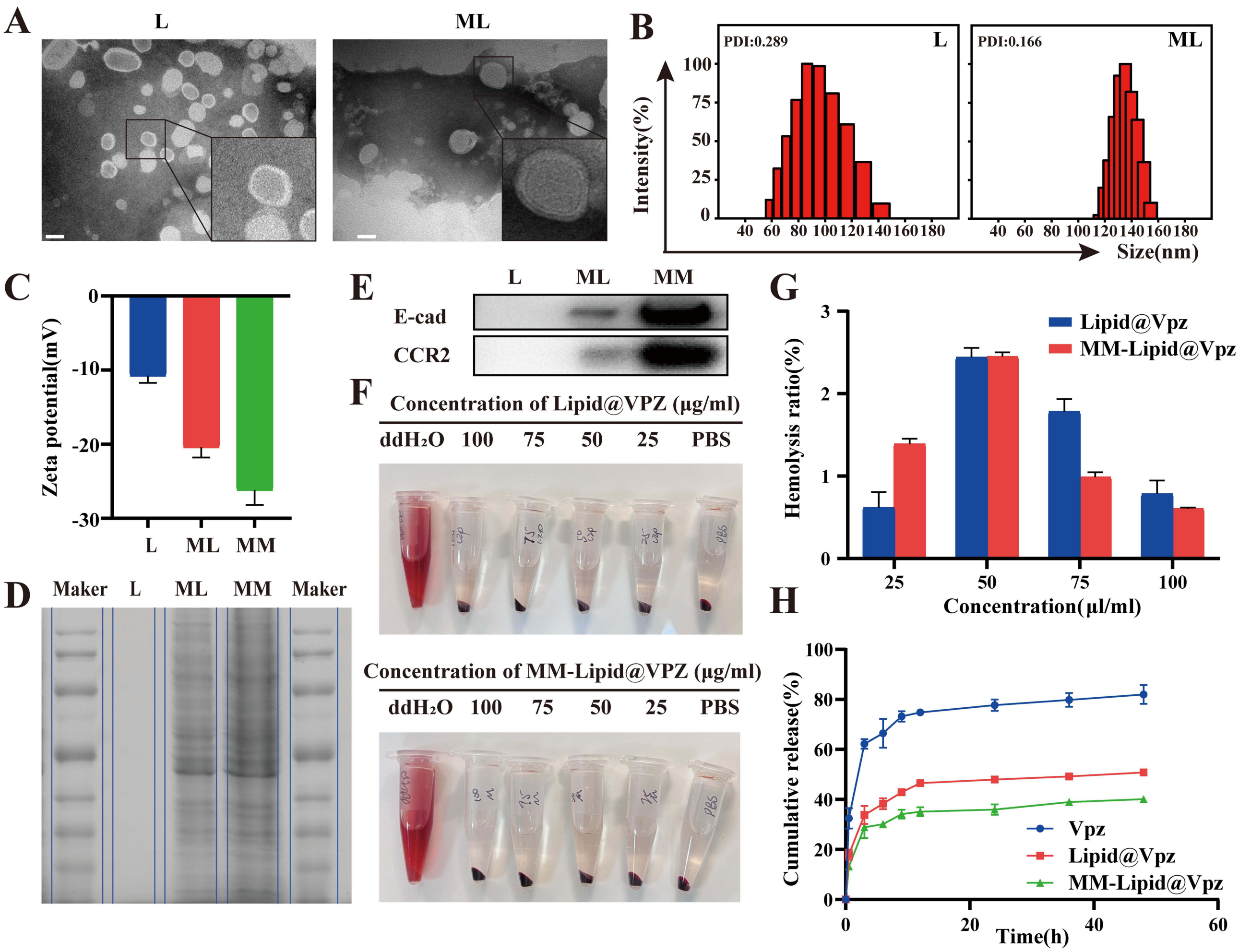

Figure 1 The construction and characterization of Lipid@Vpz and MM-Lipid@Vpz. (**A**) TEM of Lipid@Vpz and MM-Lipid@Vpz. Scale bar: 200nm. (**B**) The particle size of MM-Lipid@Vpz is 135.37 ± 12.55 nm, while that of Lipid@Vpz is 86.46 ± 26.79 nm. (**C**) The zeta potential of MM-Lipid@Vpz is −20.42 ± 1.37 mV, compared to −10.77 ± 0.95 mV for Lipid@Vpz. (**D** and **E**) Protein content on macrophage membranes determined by SDS-PAGE electrophoresis and Western blot results. (**F** and **G**) Hemolysis test for Lipid@Vpz and MM-Lipid@Vpz. (**H**) In vitro cumulative drug release of Lipid@Vpz and MM-Lipid@Vpz in PBS at pH 7.4.

at −20.42 ± 1.37 mV (Figure 1C). The encapsulation efficiencies of Lipid@Vpz and MM-Lipid@Vpz were 77.2% and 49.3%, respectively, and their drug loading rates were 5.1% and 4.5%, respectively. Moreover, SDS-PAGE electrophoresis and Western blotting verified the retention of the protein composition associated with MM in MM-Lipid@Vpz, a feature not observed in Lipid@Vpz (Figure 1D, E). These findings collectively make clear the successful modification of Lipid@Vpz with macrophage cell membranes, preserving the activity of membrane proteins.

With the intention of ruling out a killing effect of the formulation itself, the biosafety and stability of the drug are necessary considerations, and hemolysis experiments supported the evidence of excellent biocompatibility of MM-Lipid @Vpz and Lipid@Vpz (Figure 1F and G). Subsequently, within 48 hours, the in vitro drug release rate of MM-Lipid @Vpz was tested to be 40.16%, which was markedly lower than that of vonoprazan at 81.96% and Lipid@Vpz at 50.83% (Figure 1H). According to the Korsmeyer-Peppas equation, the release exponents (n) for Lipid@Vpz and MM-Lipid@Vpz were calculated to be 0.589 and 0.847, respectively. These n-values indicate a non-Fickian diffusion mechanism, meaning that the drug release does not follow purely diffusional or purely erosive behavior. Instead, it likely involves a combination of both diffusion and matrix erosion. Over time, the liposomal structure and biomimetic cell membrane are gradually disrupted in the PBS environment, thereby promoting the sustained release of the encapsulated drug into the dissolution medium. This dual mechanism contributes to a more controlled and prolonged release profile, which is desirable for therapeutic applications.

The slow-release property of MM-Lipid@Vpz contributed to a reduction in drug leakage and the potential for adverse reactions during in vivo administration, by mitigating the rapid release of the drug. Within 72 hours, neither the encapsulation efficiency nor the particle size of both showed significant changes (Figure S1A and B), indicating that the prepared liposomes possess good temporal stability. In an environment containing 10% FBS, Lipid@Vpz and MM-Lipid@Vpz remained stable within 24 hours without a significant increase in particle size (Figure S1C), demonstrating that these liposomal formulations exhibit good stability under simulated in vivo blood flow conditions.

Cellular Uptake and Antitumor Efficacy Evaluation of MM-Lipid@Vpz in Lymphoma Cells

Macrophages specifically recognize pathogen components such as bacterial lipopolysaccharide, DNA, or extracellular proteins through pattern recognition receptors, while normal cells bind to their corresponding receptors and release a "don't eat me" signal to prevent engulfment.[39] Therefore, we attempted to certify whether the macrophage membrane vesicles has a high affinity for tumor cells and can escape phagocytosis by normal macrophages. As elucidated in Figure 2A and B, after co-culturing MM-Lipid@C6 with SU-DHL-8 cells for 3, 6, and 9 hours, the intracellular fluorescence intensity was enhanced with time as assessed by flow cytometry. Specifically, the MM-Lipid@C6 group was the strongest, 1.24 times that of the Lipid@C6 group as well as 4.42 times that of the FREE-C6 group.

Given that RAW264.7 cells possess characteristics typical of murine macrophages, we also co-incubated these delivery systems with RAW264.7 cells. Consistent with the previous findings, the intracellular fluorescence intensity increased over time, demonstrate that MM-Lipid has strong targeting ability to tumor cells. However, the MM-Lipid@C6 group showed weaker fluorescence than the FREE-C6 group, while the Lipid@C6 group showed the strongest fluorescence intensity (Figure 2C).

Based on the previous results, we conjectured whether the enhancement of internalization capacity brought about the improvement of drug efficacy, in consequence, we conducted an in vitro experiment to perform a study on the antitumor efficacy of macrophage membrane vesicles against DLBCL. We selected SU-DHL-8 cells for CCK8 assay with different concentration gradients, and the results revealed that the cell viability of all three groups was concentration-dependent, in which the IC_{50} scores of Vpz and Lipid@Vpz were 145 μg/mL and 109 μg/mL. Notably, the IC_{50} scores of MM-Lipid @Vpz correspondingly declined by 76.55% and 68.81%, exhibiting the strongest cytotoxicity (Figure 2D). Besides, after co-incubating the drug for 24 hours, it was found that apoptosis was most pronounced in the MM-Lipid@Vpz group. Specifically, apoptosis in the MM-Lipid@Vpz group was 3.69-fold and 1.26-fold of the Vpz and Lipid@Vpz groups, respectively (Figure 2H and I).

The anti-apoptotic protein bcl-2 was also performed by Western blot analysis and decreased by 32.53% and 18.75% in the MM-Lipid@Vpz group compared with the Vpz and Lipid@Vpz groups. Equally, cleaved-caspase3 was most significantly up-regulated after MM-Lipid@Vpz treatment. Those results precisely demonstrates that apoptosis was most pronounced in the MM-Lipid@Vpz group, with the best effect of the drug treatment (Figure 2E). Using flow cytometry to further quantify intracellular ROS levels, the MM-Lipid@Vpz group signified a 46% and 18% growth over the Vpz and Lipid@Vpz groups, revealing greater oxidative stress and cellular damage. In general, mitochondria are the main site of ROS production, which are generated during the work of the ETCs, and excessive ROS suggest mitochondrial dysfunction, which involves OXPHOS and impaired ETCs (Figure 2F and G).

Synergistic Anti-Tumor Efficacy and Mechanistic Insights of MM-Lipid@Vpz Combined with Dox in Lymphoma

In clinical practice, the doxorubicin regimen represents a well-established therapeutic approach. This study developed a single-drug delivery system for vonoprazan, designed for combination with existing doxorubicin regimens. In consequence, we evaluated the efficacy of MM-Lipid@Vpz in combination with doxorubicin using the Drug Combination Index (CI). CI<1 indicates a synergistic effect, CI=1 indicates an additive effect, and CI>1 indicates an antagonistic effect.[40] CompuSyn analysis revealed that, at two different ratios in Figure 2J, the CI values were 0.6 and 0.2, both less than 1, indicating that the combination therapy of MM-Lipid@Vpz and Dox exhibited synergistic effects.

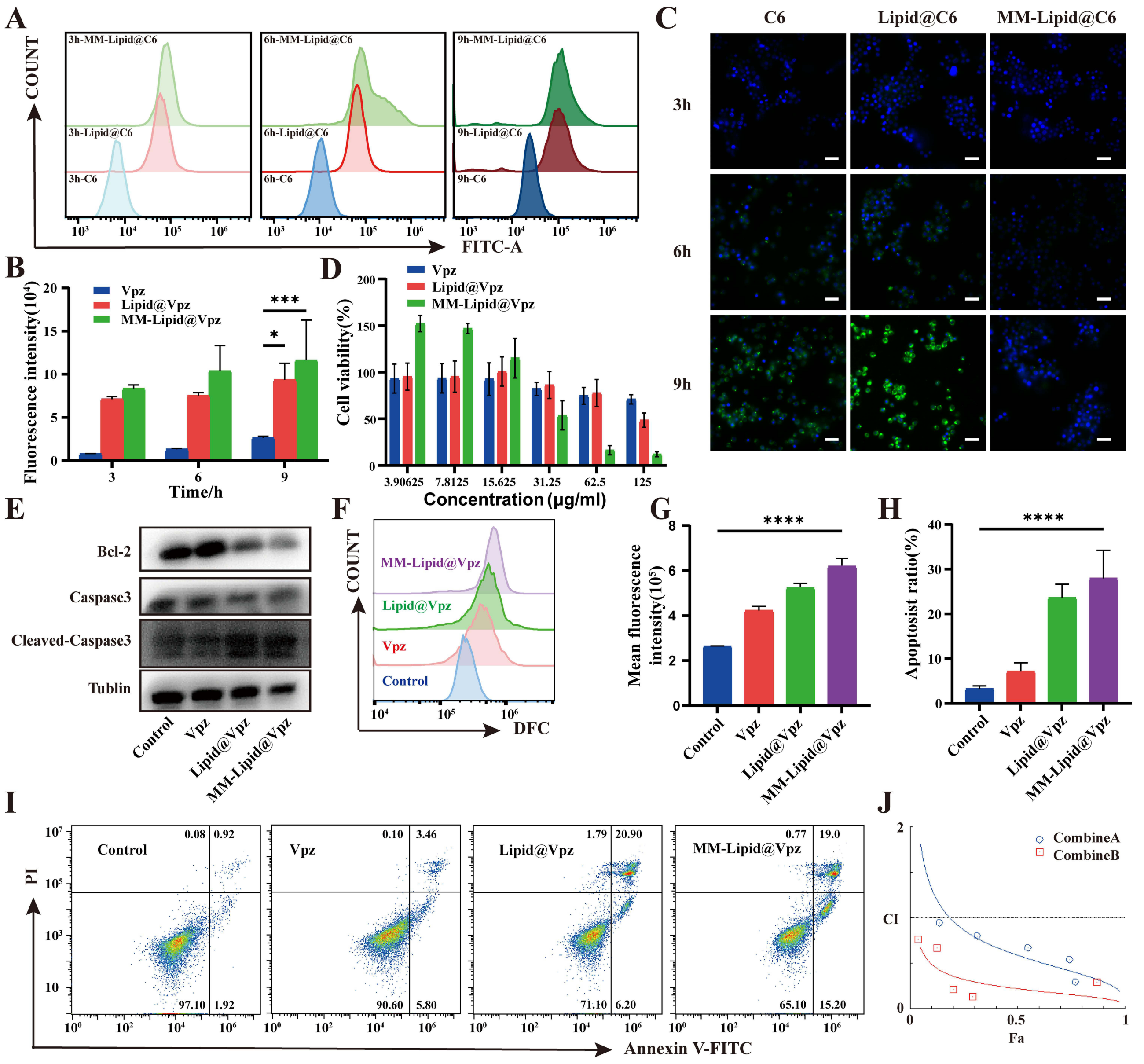

Figure 2 In vitro absorption capacity and anti-DLBCL efficacy of MM-Lipid@Vpz. (**A** and **B**) Flow cytometry analysis of fluorescent dye C6 uptake by SU-DHL-8 cells after co-incubation with Lipid@C6 and MM-Lipid@C6. (**C**) Fluorescence images showing C6 uptake by RAW264.7 cells after co-incubation with FREE-C6, Lipid@C6 and MM-Lipid@C6. Green fluorescence represents C6, blue fluorescence represents DAPI, scale bars are 50 μm. (**D**) cck8 Detection of cell survival after 24 hours of vonoprazan, Lipid@Vpz and MM-Lipid@Vpz treatment of SU-DHL-8 cells. (**E**) Western blot assessment of apoptosis-related proteins. (**F** and **G**) Quantification of intracellular reactive oxygen species levels by flow cytometry. (**H** and **I**) Quantification of apoptosis by flow cytometry. (**J**) CompuSyn software to display the inhibition rate. Combine A represents a ratio of Dox to MM-Lipid@Vpz of 1:62.5, while Combine B represents a ratio of Dox to MM-Lipid@Vpz of 1:40. Data are mean ± SD (n = 3 independent experiments; *$P < 0.05$, ***$P < 0.001$ and ****$P < 0.0001$ by one-way ANOVA).

Aiming to further validate these results, lymphoma cells were co-incubated with PBS, vonoprazan, Lipid@Vpz, MM-Lipid@Vpz, Dox, and the combination of MM-Lipid@Vpz and Dox for 24 hours. Cell viability was assessed using Calcium Xanthophyll-AM staining and there was a 20.93% and 63.96% decrease in fluorescence intensity in the combination group as compared to the two individual groups (MM-Lipid@Vpz and Dox) indicating that the efficacy of the two-drug combination was greater than that of any of the mono groups (Figure S2).

Western blot analysis confirmed that the level of anti-apoptotic protein bcl-2 was down-regulated by 18.42% in the combination group compared with the MM-Lipid@Vpz group and by 32.87% compared with the Dox group respectively, indicating the increased sensitivity of the tumor cells to the anticancer therapies. In addition, caspase3 protein level was most significantly down-regulated and cleaved-caspase3 was most significantly increased in the combination therapy group, with the ratio of caspase3 to cleaved-caspase3 down-regulated by 72.62% and 55.75%, respectively, when compared to the MM-Lipid@Vpz group and the Dox group (Figure S3). These findings point to an enhanced apoptotic process in the combination treatment group, and the efficacy of the two-drug combination was superior to that of MM-Lipid@Vpz or Dox alone.

To elucidate the mechanism of MM-Lipid@Vpz action in DLBCL, we performed a comparative transcriptome analysis of SU-DHL-8 cells treated with Lipid@Vpz and MM-Lipid@Vpz for 24 hours. Venn diagrams revealed that the two groups shared 3271 differentially expressed genes (Figure 3A). KEGG enrichment analysis of differentially expressed genes (DEGs) illustrated that differentially expressed mRNAs were affected by several key pathways, including thermogenesis, OXPHOS, cellular senescence, and cell cycle, in which OXPHOS was most significantly enriched (Figure 3B). The down-regulation of some mitochondria-related genes was more visually observed in the enrichment chord plot (Figure 3C). Subsequently, after examining all differential genes and doing heat map analysis, we found that all mitochondria-related genes involved in this sample showed consistent negative enrichment (Figure 3D), with MT-ND5, MT-CYB, MT-CO3 and MT-ATP6 again being seen most significantly by volcano plot (Figure 3F). In order to further verify the change of the above indicators, Western blotting assays were performed as exhibited in Figure 3E. In short, Results demonstrated a 66.19%, 19.41%, 43.72%, and 3.72% decrease in MT-ND5, MT-CYB, MT-CO3, and MT-ATP6 protein levels in the MM-Lipid@Vpz group compared with the Lipid@Vpz group.

Regulation Effect of MM-Lipid@Vpz on Mitochondrial OXPHOS and Energy Metabolism in Lymphoma Cells

The consistent down-regulation of MT-ND5, MT-CYB, MT-CO3 and MT-ATP6, which are significantly differentiated genes in the mitochondrial OXPHOS pathway, exposed the attenuation of cellular mitochondrial OXPHOS, suggesting that MM-Lipid@Vpz accelerates cell death by inhibiting mitochondrial OXPHOS. This is consistent with our previous MM-Lipid@Vpz pharmacodynamic experiments in which we traced that MM-Lipid@Vpz promotes apoptosis and oxidative stress and involves impaired mitochondrial OXPHOS. To further validate this, we did more specific experiments.

Seeking to changes in the level of mitochondrial OXPHOS, we utilized the Seahorse XF extracellular flux analyzer,[41] a robust tool for assessing mitochondrial OXPHOS. Considering that oxygen consumption is primarily associated with mitochondrial OXPHOS, the real-time OCR serves as a critical metric reflecting mitochondrial respiratory efficiency and functional status. The data demonstrated a significant decrease in the MM-Lipid@Vpz group (Figure 4A). Additionally, other key indicators, such as basal respiration, ATP-linked respiration, proton leak, and maximal respiration, also reflected a marked reduction (Figure 4B). In the mitochondrial stress test, the decrease in basal respiration is based on the diminished basic metabolic activity of the cell. Whereas ATP-linked respiration is the state in which ATP produced from consumed substrates is associated with the process of OXPHOS and represents the efficiency of OXPHOS, reduced ATP-linked respiration also implies that the cell is less efficient at converting metabolic substrates to ATP. What's more, proton leakage is a phenomenon in which protons pass directly through the inner mitochondrial membrane without passing through the enzyme ATP synthase, which means that some of the energy is not being utilized efficiently. While a drop in proton leakage is in some ways indicative of an increase in the efficiency of energy conversion from one point of view, it may reveal a weakening of the mitochondria's ability to regulate proton dynamics if it is decreased in conjunction with other metrics. Last but not least, maximal respiration is a reflection of the cell's metabolic capacity, and its diminution signals a weakening of the cell's adaptive capacity in the face of high metabolic demands. Briefly, MM-Lipid@Vpz did cause severe mitochondrial OXPHOS.

Furthermore, the intracellular NAD^+/NADH ratio and ATP content were notably diminished in the MM-Lipid@Vpz group, with a decrease of 22.55% in the NAD^+/NADH ratio, 14.16% in ATP content, compared with group Lipid@Vpz (Figure 4E and F). NADH acts as an electron donor, driving the ETCs and generating ATP to energize the cell through the action of the proton pump. And our results detected a decrease in them, which certainly releases a signal that the balance of the ETCs is broken. The ETCs can be seen as a driver of OXPHOS, which depends on the proton gradient established by the ETCs. Since the mitochondrial membrane potential embodied the activity of the proton pump,[42] treatment of the cells with

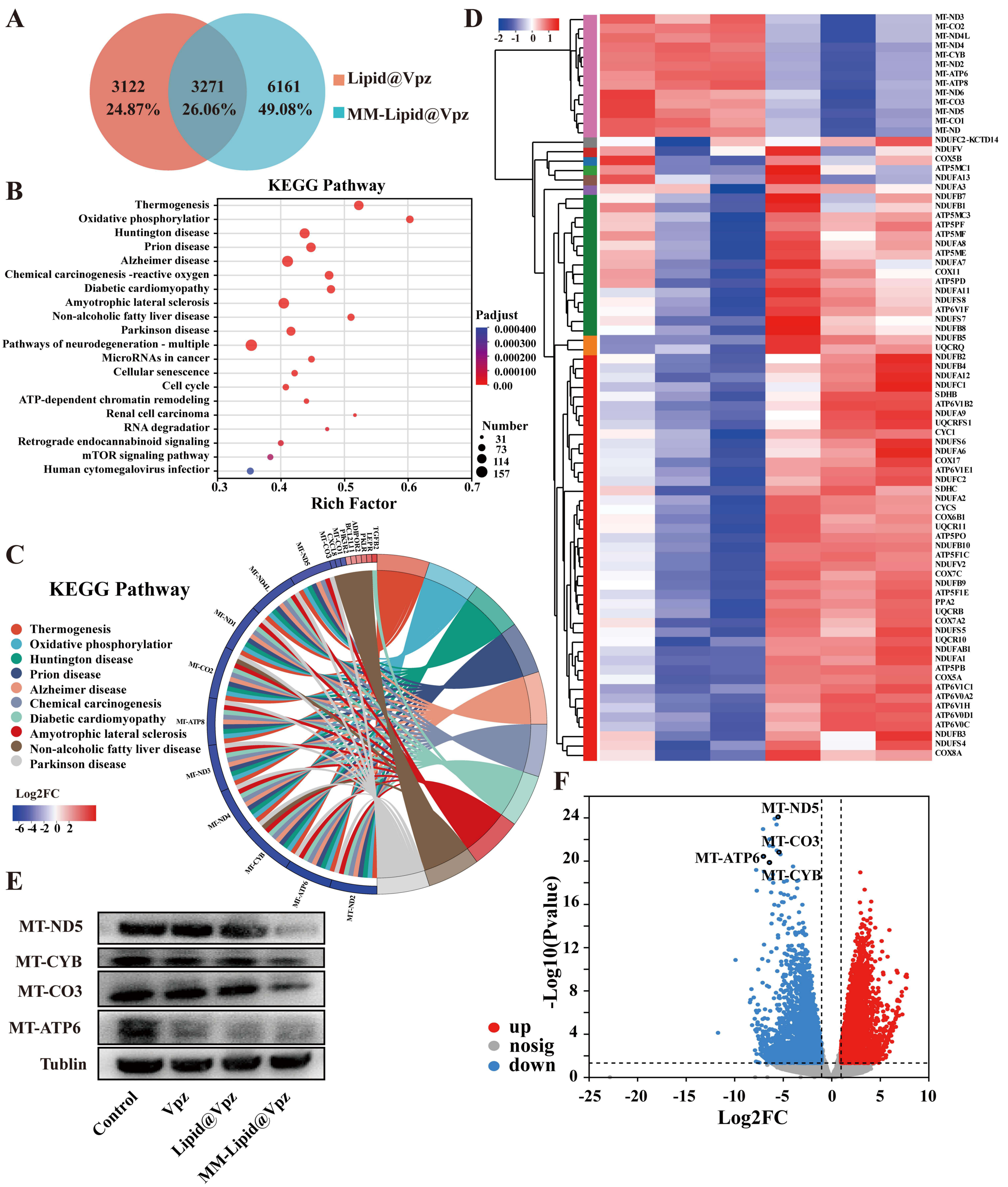

Figure 3 Mechanism of anti-DLBCL action of MM-Lipid@Vpz. (**A**) Intersection of two sample genes by using Venn diagram. The Orange part is group Lipid@Vpz, the blue part is group MM-Lipid@Vpz. Intersections are genes that are the same in both samples. (**B**) KEGG enrichment analysis of signaling pathways. (**C**) Enrichment chordal maps visualize the signaling pathways and differential genes enriched in both samples. (**D**) Generating heat maps from differentially oxidatively phosphorylated genes. (**E**) Western blot analysis of MT-ND5, MT-CYB, MT-CO3 and MT-ATP6 expression in each group. (**F**) Volcano plot showing representative differential genes.

the JC-1 fluorescent probe manifested a significant decrease in the mitochondrial membrane potential in the MM-Lipid @Vpz group, which was 1.31 times higher than that in the Lipid@Vpz group (Figure 4C and D). Together, these results support that ETCs dysfunction and thus mitochondrial OXPHOS dysfunction can be inferred.

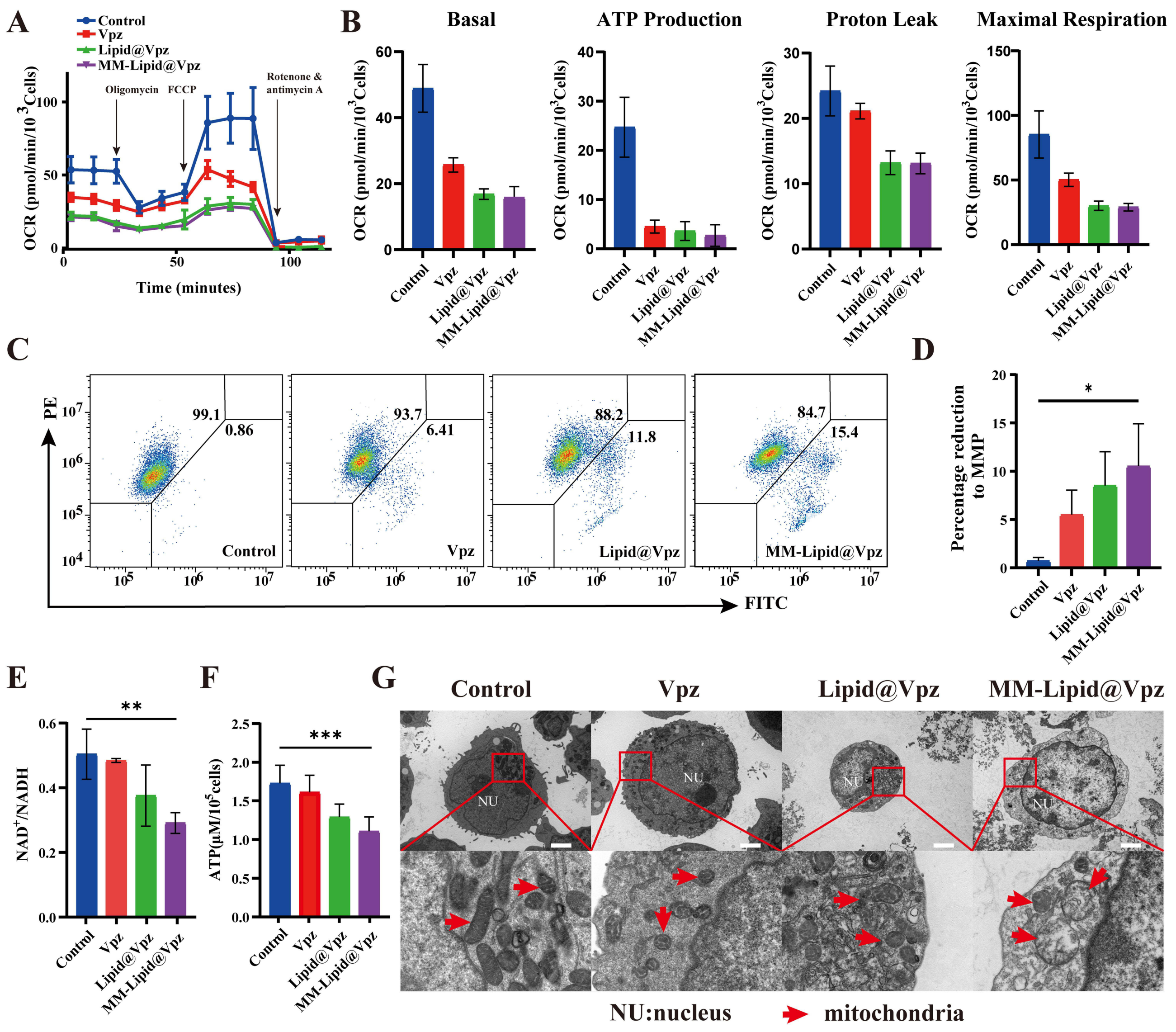

Figure 4 Mechanism of action of MM-Lipid@Vpz affecting cellular OXPHOS. (**A**) Real-time OCR was measured in each group using a Seahorse XF 24 analyzer. (**B**) Quantification of basal respiration, proton leak rate maximal respiration, ATP production coupled respiration and maximal respiration. Data are shown as mean ± SEM. (**C** and **D**) Detection of mitochondrial membrane potential levels by flow cytometry. (**E**) Determination of NAD$^+$/NADH ratio for each group. (**F**) Determination of ATP content in each group. (**G**) SU-DHL-8 cell TEM image, NU: nucleus; red arrow: mitochondria; scale bar: 5µm. Data are mean ± SD (n = 3 independent experiments; $^{*}P < 0.05$, $^{**}P < 0.01$, $^{***}P < 0.001$ and by one-way ANOVA).

OXPHOS mainly occurs in the inner membrane of mitochondria, which contains a series of important enzyme complexes and ETCs, and direct observation of mitochondrial morphology can visually detect changes in OXPHOS,[43] TEM images displayed that mitochondrial cristae were significantly scaled down in the MM-Lipid @Vpz group, significantly shrinking the surface area of the membrane and allowing a more limited number of OXPHOS reactions to take place; mitochondria appeared to be swollen as an indication of adapting to the reduced energy demand; and the presence of more apoptotic vesicles in the nucleus instructed the cells to be undergoing apoptosis (Figure 4G). Together, the above findings point to the fact that MM-Lipid@Vpz inhibits OXPHOS by targeting the mitochondrial ETCs, which leads to impaired energy production and increased apoptosis, in turn exerting an antiproliferative effect on lymphoma cells.

In vivo Evaluation of Enhanced DLBCL Tumor Targeting and Anti-Tumor Efficacy by MM-Lipid@Vpz

To assess the in vivo targeting ability of MM-Lipid@Vpz against DLBCL, we established a subcutaneous tumor model in nude mice, and near-infrared fluorescent probe IR780 labelled MM-Lipid was injected by tail vein and monitored in real time (Figure 5A). Twenty-four hours after injection, the MM-Lipid@IR780 group exhibited the strongest fluorescence intensity, which was 60.10% and 37.32% higher than that of the IR780 group and the Lipid@IR780 group (Figure 5B and D). We then dissected the DLBCL model nude mice and the MM-Lipid@IR780 group had the strongest fluorescence signal as expected. In addition, the fluorescence signal of the Lipid@IR780 and MM-Lipid@IR780 groups mainly clustered at the tumor site rather than the main organs, and fluorograms demonstrate that fluorescent signals can be observed in the lungs of the IR780 group that are not present in the other two groups (Figure 5C and E). These phenomena reflect the focused targeting ability of liposomes and biofilm vesicles on tumors. To verify whether MM-Lipid@Vpz can evade phagocytosis by macrophages in vivo, we co-incubated BMDMs with C6-labeled MM-Lipid. Under a fluorescence microscope, we observed that the MM-Lipid@C6 group exhibited almost undetectable fluorescence signals, whereas the Lipid@C6 group reached its peak fluorescence intensity at 9 hours, surpassing that of all other groups (Figure S4). Overall, liposomes and modified liposomes had stronger tumor targeting properties, and the presence of macrophage membranes significantly improved the target specificity of the delivery system.

For investigating the in vivo antitumor efficacy of MM-Lipid@Vpz, we randomly divided nude mice into four groups by their subcutaneous tumor model and treated them with saline, vonoprazan, Lipid@Vpz and MM-Lipid@Vpz on days 1, 3, 5, 7, 9, 11 and 13 (Figure 6A). Body weights and tumor sizes were recorded every two days post-treatment, and the mice were euthanized on day 15 for tumor excision and analysis (Figure 6B). In four groups of mice, tumor volume and weight were reduced by 77.67% and 74.56% in the MM-Lipid@Vpz group compared to the control group, strongly demonstrating its significant therapeutic effect. Similarly, there was a small decrease in tumor volume and weight in the Vpz and Lipid@Vpz groups, which specifically reached to 17.82% and 8.35% in the Vpz group, while it went to 40.15% and 45.70% in the Lipid@Vpz group, respectively (Figure 6D). Furthermore, the tumor growth curves displayed that tumor in the normal saline group grew the fastest, while the MM-Lipid@Vpz group grew the slowest (Figure 6E). These results collectively demonstrate that MM-Lipid@Vpz significantly inhibits tumor growth in DLBCL lymphoma model nude mice.

Histopathological analysis using HE, Ki67 and TUNEL staining was performed to assess tumor damage and necrosis, proliferation and apoptosis. In the MM-Lipid@Vpz group, we observed the most significant necrotic areas. Additionally, the number of Ki67-positive cells in this group was significantly lower, indicating a greater degree of inhibition of cell proliferation activity. Furthermore, the TUNEL fluorescence signal in this group was also significantly higher than in other treatment groups, further confirming the severity of apoptosis. These results collectively suggest that MM-Lipid @Vpz treatment may have a strong damaging effect on cells, leading to increased cell necrosis and apoptosis, as well as a decrease in cell proliferation capacity (Figures 6F and 7A). Western blot analysis of tumor tissues revealed that the expression of apoptosis-related proteins was consistent with the results of in vitro experiments. Compared to the Vpz and Lipid@Vpz groups, the MM-Lipid@Vpz group showed a downregulation of bcl-2 protein by 65.19% and 31.94%, respectively, while the ratio of caspase3 to cleaved-caspase3 was reduced by 79.60% and 43.48% (Figure 7B). This confirms that MM-Lipid@Vpz indeed exhibits superior antitumor efficacy.

It is worth noting that during the overall treatment period, there were no significant differences between groups in mouse body weights (Figure 6C), indicating good in vivo safety profile. Additionally, the major organs of the mice were isolated and subjected to HE staining, all of which showed no significant pathological changes (Figure 6H), and same was true for the blood samples, which were free of abnormal changes in the levels of RBC, WBC, PLT, ALT, AST, BUN, and CREA (Figure 6G). Figure S8 shows the normal reference range for each indicator. Consequently, MM-Lipid@Vpz can exhibit antitumor effects without inducing additional toxicity.

To further verify our hypothesis, we subjected tumor sections to ROS staining, and Figure 7C informs us that the MM-Lipid@Vpz group presented the strongest fluorescence compared to the other groups. From the immunohistochemical results, it can be discerned that the expression level of MT-CYB and MT-ATP6 protein is notably the lowest in the MM-Lipid

https://doi.org/10.2147/IJN.S520567

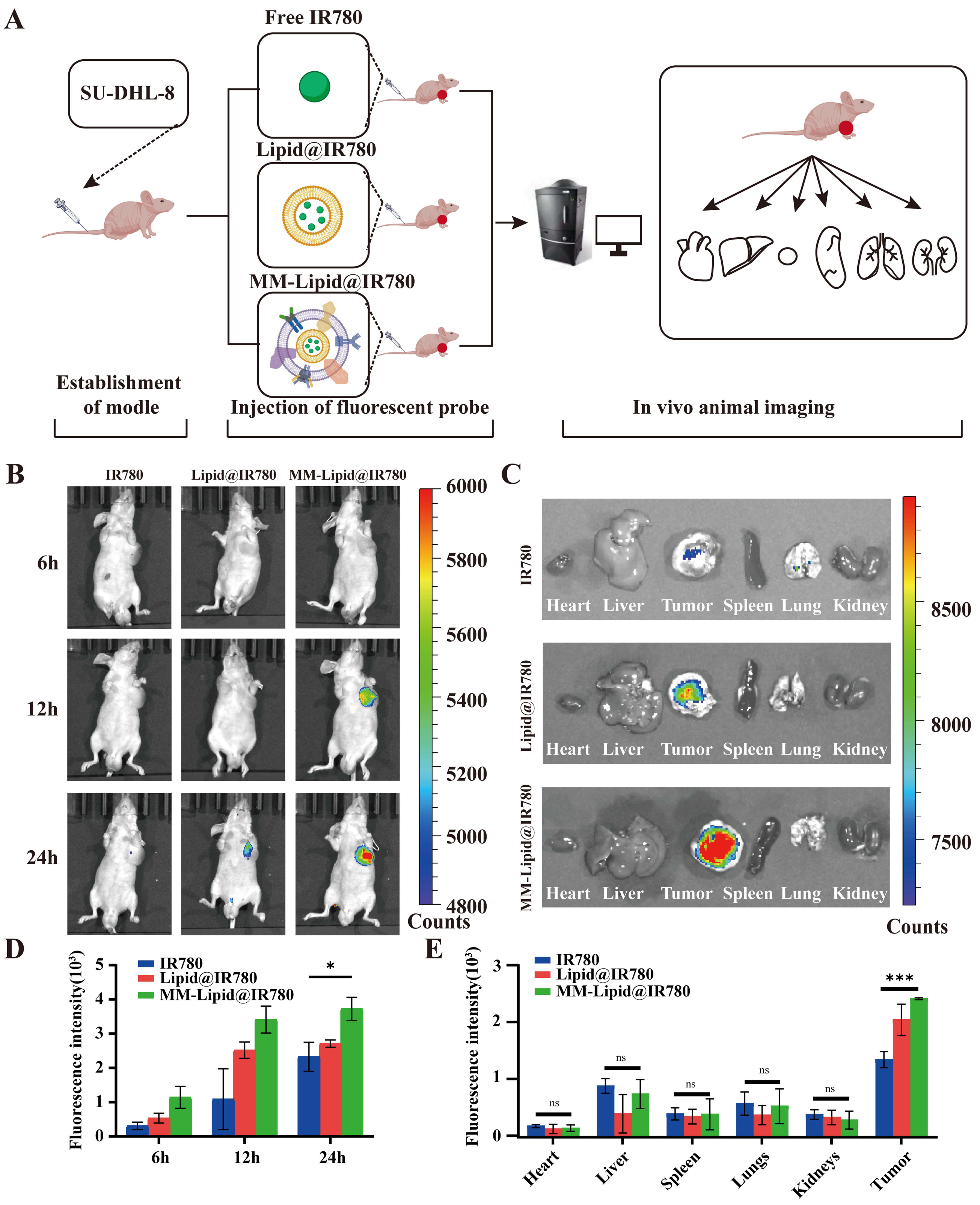

Figure 5 In vitro absorption capacity of MM-Lipid@Vpz. (**A**) Schematic of in vivo imaging for this study. To assess the distribution of the delivery system in vivo, fluorescence imaging was performed on mice at different times after intravenous injection. (**B**) Fluorescence imaging of nude mice 6, 12 and 24 hours after injection of FREE-IR780, Lipid@IR780L and MM-Lipid@IR780. (**C**) Fluorescence imaging of dissected groups of major organs and tumors. (**D**) Quantitative fluorescence analysis of post-injection nude mice at various time intervals. (**E**) Quantification of fluorescence intensity of hearts, livers, spleens, lungs, kidneys and tumors 24 hours after injection in FREE-IR780, Lipid@IR780 and MM-Lipid@IR780 groups. Data are mean ± SD (n = 3 mice per group); *P < 0.05, ***P < 0.001 and by one-way ANOVA.

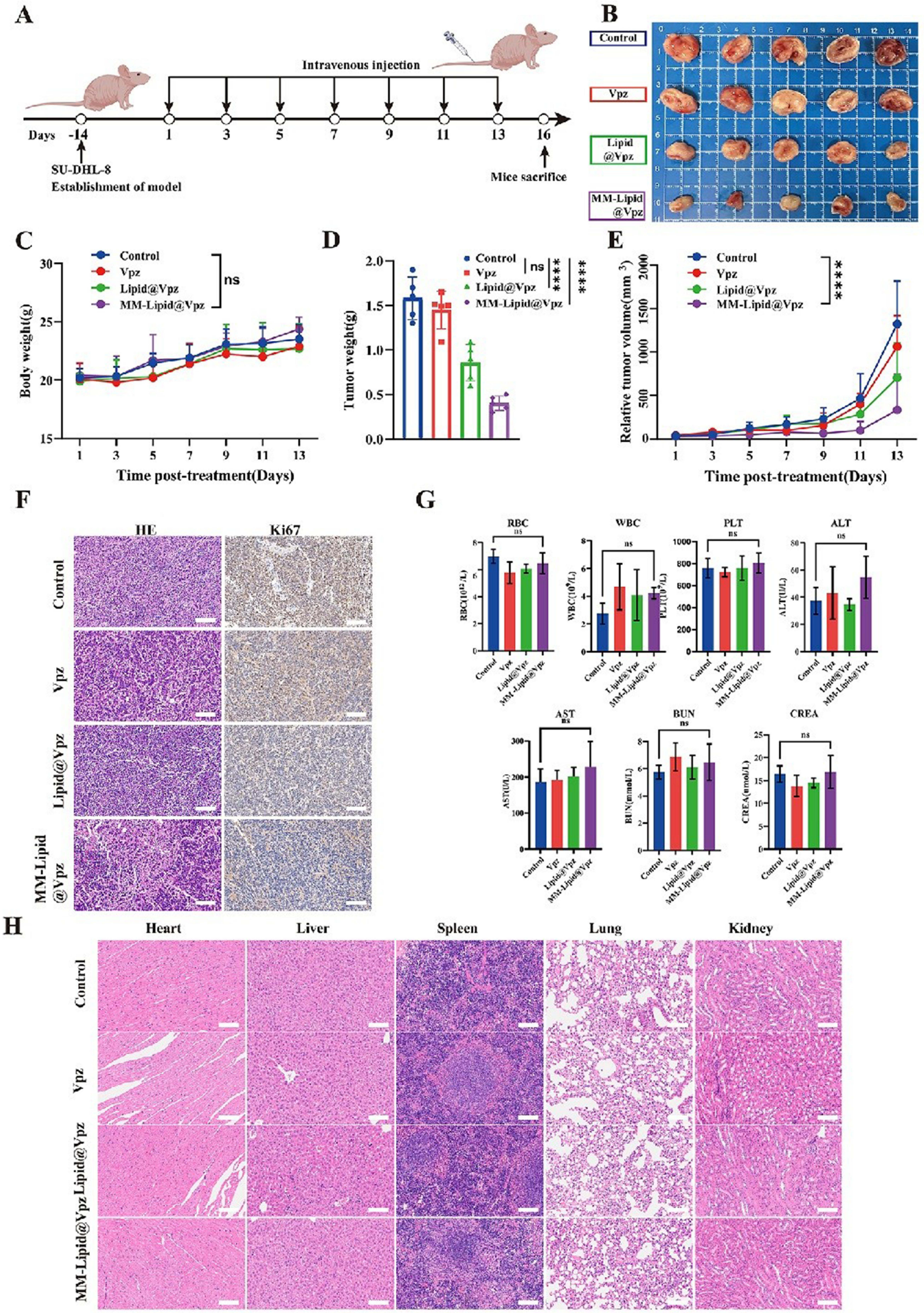

Figure 6 MM-Lipid@Vpz in vivo anti-DLBCL efficacy. (**A**) Establishment of nude mouse DLBCL subcutaneous tumor model and schematic diagram of drug treatment plan. (**B**) Photographs of tumor anatomy for all groups. (**C**) Body weight curve of mice after starting treatment. (**D**) Tumor weights in mice glassed down. (**E**) Tumor volume curve in mice after starting treatment. (**F**) HE and Ki67 staining of mouse tumor tissue, scale bars are 50 μm. (**G**) RBC, WBC, PLT, ALT, AST, BUN, CREA of mice in control, Vpz, Lipid@Vpz and MM-Lipid@Vpz groups are shown as bar graphs. (**H**) HE staining of heart, liver, spleen, lungs, and kidneys of mice in control, Vpz, Lipid@Vpz and MM-Lipid @Vpz groups, and the scale bars are 50 μm. Data are mean ± SD (n = 5 mice per group); ****P < 0.0001 by one-way ANOVA.

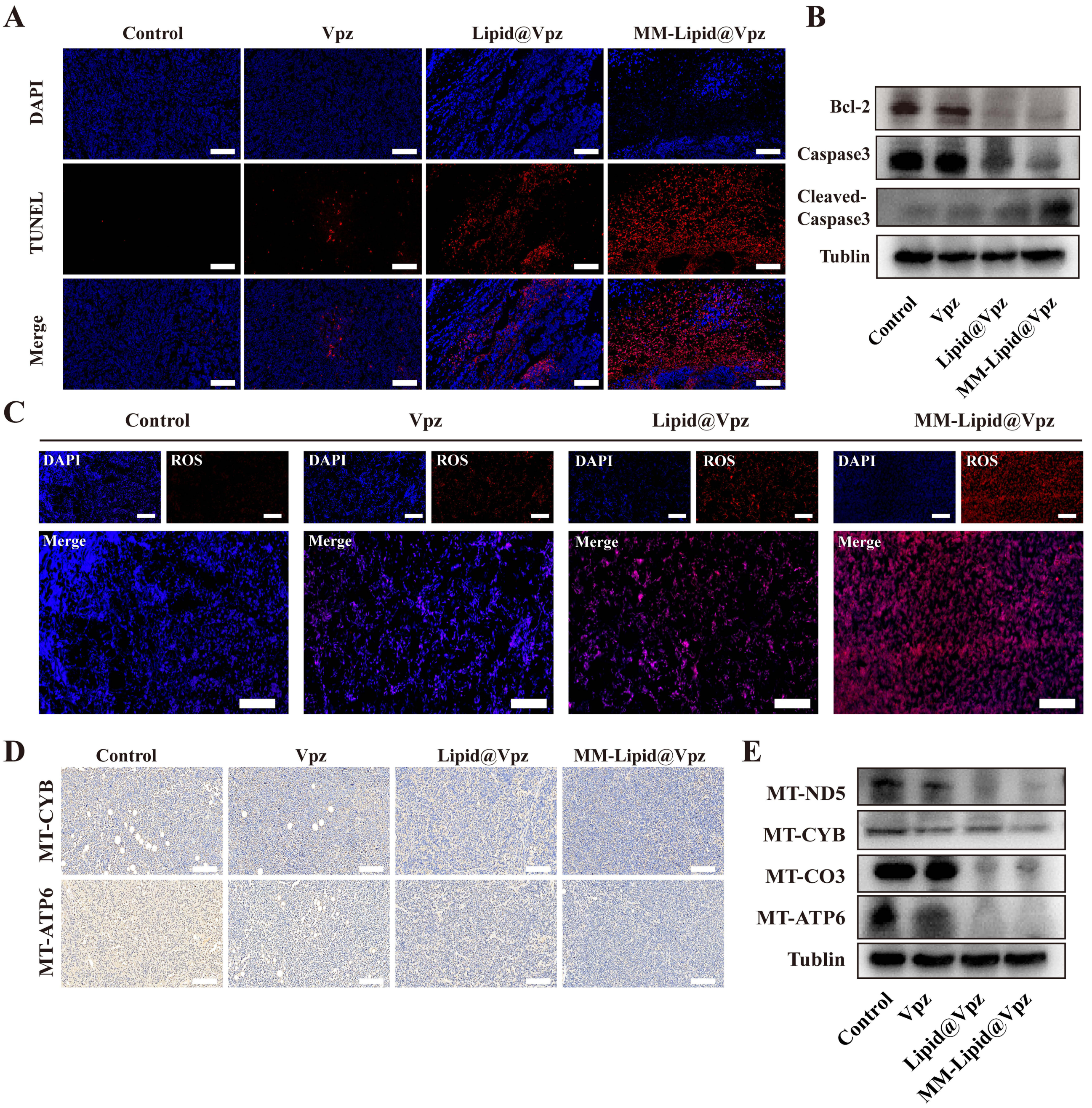

Figure 7 The anti-DLBCL mechanism of MM-Lipid@Vpz in vivo (**A**) TUNEL staining of mouse tumor tissue, scale bars are 50 μm. (**B**) Western blot analysis of apoptosis-related proteins in tumor tissues of the control, Vpz, Lipid@Vpz, and MM-Lipid@Vpz groups. (**C**) ROS staining of mouse tumor tissue, scale bars are 50 μm. (**D**) The immunohistochemical analysis of the expression levels of MT-ND5, MT-CYB, MT-CO3 and MT-ATP6 in each group of tumor tissues, scale bars are 50 μm. (**E**) Western blot analysis of the expression levels of MT-ND5, MT-CYB, MT-CO3 and MT-ATP6 in each group of tumor tissues.

@Vpz group (Figure 7D). Congruently, Western blotting analysis reveals a consistent downregulation trend in the expressions of MT-ND5, MT-CYB, MT-CO3, and MT-ATP6 proteins within tumor tissues compared to prior findings. Specifically, within the MM-Lipid@Vpz cohort, the expressions of MT-ND5, MT-CYB, MT-CO3, and MT-ATP6 proteins exhibit reductions of 10.93%, 19.16%, 31.07%, and 34.63%, respectively, relative to the Lipid@Vpz group (Figure 7E). This supports that MM-Lipid@Vpz achieves its in vivo antitumor efficacy by inhibiting the OXPHOS pathway.

In summary, these in vivo studies provide strong evidence that MM-Lipid@Vpz significantly inhibits tumor growth, induces oxidative stress, and has a favorable biosafety profile. Therefore, it is expected to be a candidate for lymphoma treatment.

Synergistic Anti-Tumor Effects and Safety Profile of MM-Lipid@Vpz Combined with Dox in vivo

Inhibition of OXPHOS synergistically increases the efficacy of first-line antitumor drugs,[44] and our previous results demonstrated the good antioxidant phosphorylation effect of MM-Lipid@Vpz, based on which, it occurred to us whether MM-Lipid@Vpz can synergize with Dox to treat DLBCL in vivo. We then set up a subcutaneous tumor model in nude mice and administered saline, MM-Lipid@Vpz, Dox, or a combination of MM-Lipid@Vpz and Dox in the same mode of administration as before (Figure 8A). As seen in Figure 8B, MM-Lipid@Vpz treatment in combination with Dox successfully inhibited tumor growth, with tumor inhibition rates of more than 70% compared to either monotherapy (Figure 8D and E). The body weights of each group of mice, especially when compared with the control group, showed no significant differences (Figure 8C), suggesting that no severe gastrointestinal toxicity, liver and kidney failure, or serious infections and other toxicities were caused, thus confirming the safety of the preparation. Tumor tissues were collected for HE, Ki67 and TUNEL staining, and the combination treatment group also demonstrated more cellular damage and less Ki67-positive cells (Figure S5). In addition, the TUNEL fluorescence signals manifested that the positive areas of both MM-Lipid@Vpz and Dox groups were sparser than those of MM-Lipid@Vpz+Dox group (Figure S6). In the Western blot analysis of tumor tissues, the bcl-2 protein level in the combination therapy group decreased by 61.07% compared to the MM-Lipid@Vpz group and by 35.02% compared to the Dox group. Meanwhile, the ratio of caspase-3 to cleaved-caspase-3 in the combination therapy group decreased by 67.85% and 40.42% respectively compared to the MM-Lipid@Vpz group and the Dox group. The combination therapy group significantly enhanced the apoptosis process of tumor cells, demonstrating a stronger antitumor effect than single treatments (Figure S7). Last but not least, no abnormalities were found in the tests of major organs and blood samples of nude mice, which ensured that in our treatment, mice in all groups did not exhibit organ damage or hematological toxicity, which confirms the good biosafety of the combination therapy (Figure 8F and G). On the whole, these results revealed that MM-Lipid@Vpz can safely and effectively synergize with Dox, which may be effective in mitigating the phenomenon of drug resistance and toxic side effects.

Discussion and Conclusion

DLBCL is characterized by a significant heterogeneity in cellular energy metabolism, which has profound implications for the development of targeted therapies.[45] The metabolic profile of DLBCL can be dichotomized into pathways that favor aerobic glycolysis and those that rely on OXPHOS.[46] This study underscores the importance of regulating mitochondrial function in DLBCL, particularly the role of OXPHOS in tumor growth, as well as the potential therapeutic benefit of targeting this pathway.

By using potassium-competitive acid blockers (P-CABs), such as vonoprazan which is typically targeted at the proton pump of gastric parietal cells, we demonstrated its indirect impact on mitochondrial ATP homeostasis and energy metabolism in lymphoma cells. However, the high plasma protein binding rate of vonoprazan prevents it from concentrating in non-gastric cells. Mitochondrial membrane drug delivery systems can achieve targeted binding through the electrostatic interaction between cationic liposomes and the negatively charged mitochondrial membrane.[47,48] Another study utilized photosensitive hydrogels to generate reactive oxygen species under specific wavelength light, which disrupt the mitochondrial membrane structure, thereby triggering drug release.[49,50] However, this method may interfere with mitochondrial membrane integrity and induce cellular stress responses, meanwhile, is prone to degradation or phagocytosis by the phagocytic system during circulation in in vivo. Liposome-encapsulated doxorubicin has been used in the clinical treatment of lymphoma,[51] but it is easily cleared due to factors such as binding to plasma proteins and immune recognition. Studies have shown that liposomes coated with macrophage membranes can effectively target spinal cord injuries.[52] Based on this, this study designed a biomimetic formulation derived from macrophage membranes to evade phagocytosis by macrophages. Bionic macrophage membranes retain complete proteins, including surface proteins for tumor recognition (such as CD44, TLRs) and molecules for immune escape (such as PD-L1, CD200),[53,54] while masking antigens to reduce immune recognition.

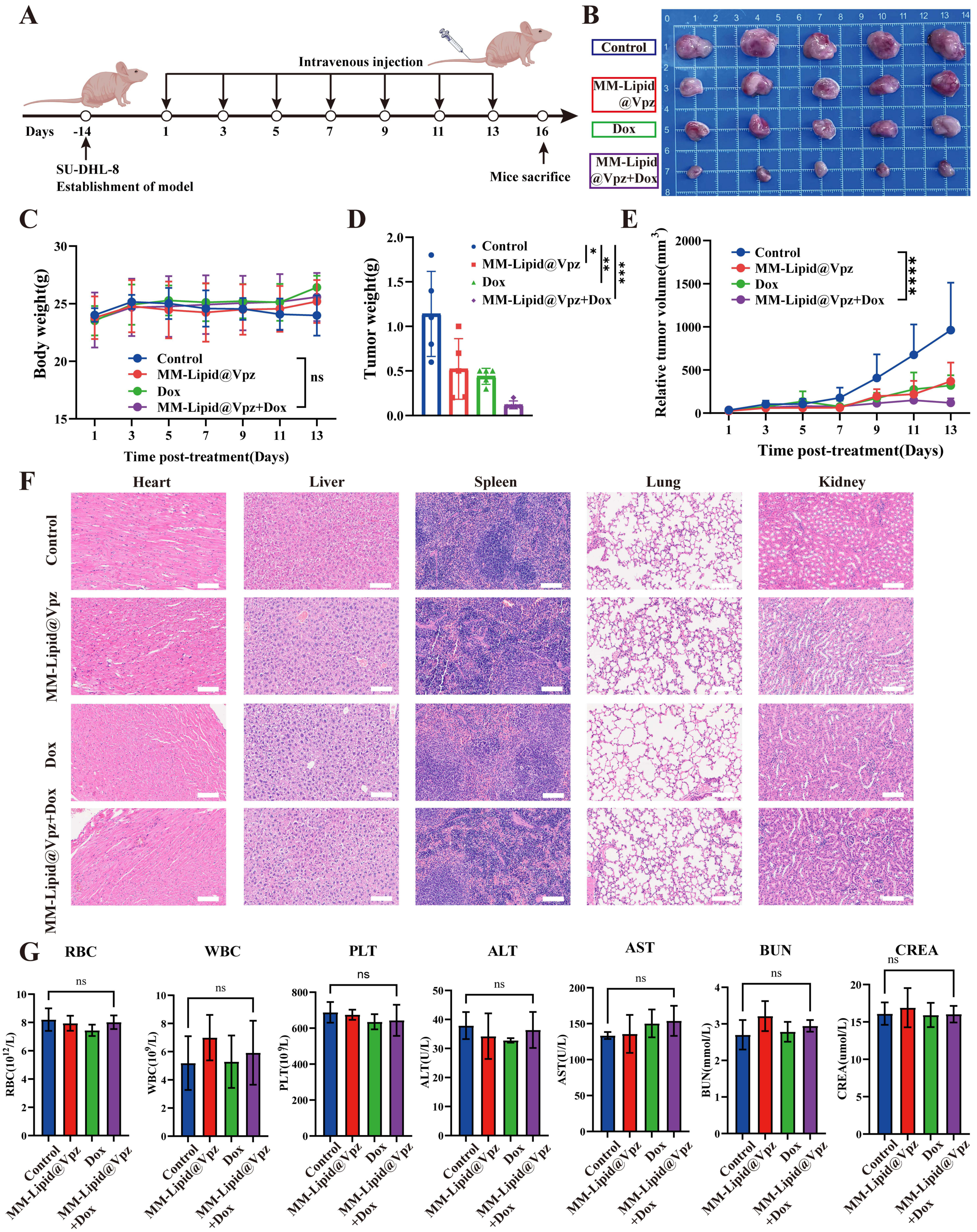

Figure 8 Efficacy of MM-Lipid@Vpz in combination with Dox for in vivo anti-DLBCL treatment. (**A**) Establishment of nude mouse DLBCL subcutaneous tumor model and schematic diagram of drug treatment plan. (**B**) Tumor reveal photos for all groups. (**C**) Body weight curve of mice after starting treatment. (**D**) Tumor weights in mice glassed down. (**E**) Tumor volume curve in mice after starting treatment. (**F**) HE staining of heart, liver, spleen, lungs, and kidneys of mice in control, MM-Lipid@Vpz, Dox and MM-Lipid@Vpz+Dox groups, and the scale bars are 50 μm. (**G**) RBC, WBC, PLT, ALT, AST, BUN, CREA of mice in control, MM-Lipid@Vpz, Dox and MM-Lipid@Vpz+Dox groups are shown as bar graphs. Data are mean ± SD (n = 5 mice per group); *P < 0.05, **P < 0.01, ***P < 0.001 and ****P < 0.0001 by one-way ANOVA.

Both in vitro and in vivo studies have confirmed that MM-Lipid@Vpz has good biocompatibility. It interferes with the mitochondrial OXPHOS process, disrupts the stability of the electron transport chain, and induces metabolic stress and apoptosis in tumor cells. This suggests that regulating mitochondrial OXPHOS may be a potential strategy for optimizing metabolic therapy in DLBCL. Additionally, the combination of MM-Lipid@Vpz and doxorubicin exhibits synergistic cytotoxicity, significantly enhancing the tumor suppression effect, indicating that this combined strategy may serve as a complementary approach to the current standard treatment for DLBCL. From the perspective of clinical translation, this study chose to develop a single-drug nanocarrier system for vonoprazan, aiming to be used in combination with the currently widely used doxorubicin-based regimens for the treatment of diffuse large B-cell lymphoma (DLBCL). Doxorubicin, as a backbone chemotherapy drug, has well-defined pharmacokinetics, dosing regimens, and safety profiles in clinical practice. Maintaining the current administration form is compatible with standard treatment protocols. The development of dual-drug nanomaterials, especially those encapsulating hydrophilic doxorubicin and lipophilic vonoprazan, faces challenges such as drug interactions, mismatched release kinetics, loading uniformity, and long-term stability, which may affect reproducibility and scalability. Additionally, the combination strategy of vonoprazan and doxorubicin based on a novel delivery system can independently control the dose, route, and sequence of the two drugs, optimize the management of synergistic toxicity, and support individualized dosing.[55] Overall, this "delivery system + existing regimen" approach strikes a balance between innovation and practicality, aiming to enhance therapeutic efficacy while reducing barriers to clinical application.

In conclusion, our research results indicate that the use of MM-Lipid@Vpz targeting mitochondrial OXPHOS provides a therapeutic strategy for DLBCL. This approach exploits the inherent metabolic vulnerability of DLBCL cells, enhances tumor targeting and apoptosis induction capabilities, while maintaining safety. The application of the biomimetic macrophage membrane-coated liposome delivery system may have implications beyond DLBCL for anticancer therapy. It should be noted that this study has certain limitations, including the lack of long-term toxicity data (such as safety observations for more than 3 months) and the absence of validation of therapeutic efficacy using in situ tumor models. The reliability of the conclusion can be strengthened by conducting larger-scale in vivo experiments with an increased number of mice. Subsequent studies will address these deficiencies and further explore the chronic safety of the formulation and its therapeutic effect in in situ models.

Ethics Statement

This animal research was approved by the Experimental Animal Management Ethics Committee of Nanjing Drum Tower Hospital (2025AE01023).

Author Contributions

All authors made a significant contribution to the work reported, whether that is in the conception, study design, execution, acquisition of data, analysis and interpretation, or in all these areas; took part in drafting, revising or critically reviewing the article; gave final approval of the version to be published; have agreed on the journal to which the article has been submitted; and agree to be accountable for all aspects of the work.

Funding

This project was supported by grants from the National Natural Science Foundation of China (Grant Nos. 82102917 to Y. Z.); Nanjing Medical Science and Technology Development Program (YKK23104 to Y.Z.). This research was supported by National Key Clinical Specialties Construction Program.

Disclosure

The authors declare no conflicts of interest in this work.

References

1. Schmitz R, Wright GW, Huang DW, et al. Genetics and pathogenesis of diffuse large B-Cell lymphoma. *N Engl J Med*. 2018;378:1396–1407. doi:10.1056/NEJMoa1801445

2. Poletto S, Novo M, Paruzzo L, et al. Treatment strategies for patients with diffuse large B-cell lymphoma. *Cancer Treat Rev*. 2022;110:102443. doi:10.1016/j.ctrv.2022.102443
3. Locke FL, Miklos DB, Jacobson CA, et al. Axicabtagene Ciloleucel as second-line therapy for large B-Cell Lymphoma. *N Engl J Med*. 2022;386:640–654. doi:10.1056/NEJMoa2116133
4. Sehn LH, Salles G. Diffuse Large B-Cell Lymphoma. *N Engl J Med*. 2021;384:842–858. doi:10.1056/NEJMra2027612
5. Danzi F, Pacchiana R, Mafficini A, et al. To metabolomics and beyond: a technological portfolio to investigate cancer metabolism. *Signal Transduct Target Ther*. 2023;8:137. doi:10.1038/s41392-023-01380-0
6. Pi M, Kuang H, Yue C, et al. Targeting metabolism to overcome cancer drug resistance: a promising therapeutic strategy for diffuse large B cell lymphoma. *Drug Resist Updat*. 2022;61:100822. doi:10.1016/j.drup.2022.100822
7. Rink JS, Yang S, Cen O, et al. Rational targeting of cellular cholesterol in diffuse large B-Cell Lymphoma (DLBCL) enabled by functional Lipoprotein nanoparticles: a therapeutic strategy dependent on cell of origin. *Mol Pharm*. 2017;14:4042–4051. doi:10.1021/acs.molpharmaceut.7b00710
8. Jiang D, Mo Q, Sun X, et al. Pyruvate dehydrogenase kinase 4-mediated metabolic reprogramming is involved in rituximab resistance in diffuse large B-cell lymphoma by affecting the expression of MS4A1/CD20. *Cancer Sci*. 2021;112:3585–3597. doi:10.1111/cas.15055
9. Zhang L, Yao Y, Zhang S, et al. Metabolic reprogramming toward oxidative phosphorylation identifies a therapeutic target for mantle cell lymphoma. *Sci Transl Med*. 2019;11.
10. Yap TA, Daver N, Mahendra M, et al. Complex I inhibitor of oxidative phosphorylation in advanced solid tumors and acute myeloid leukemia: Phase I trials. *Nat Med*. 2023;29:115–126. doi:10.1038/s41591-022-02103-8
11. Liu Y, Kimpara S, Hoang NM, et al. EGR1-mediated metabolic reprogramming to oxidative phosphorylation contributes to ibrutinib resistance in B-cell lymphoma. *Blood*. 2023;142:1879–1894. doi:10.1182/blood.2023020142
12. Peppicelli S, Bianchini F, Calorini L. Extracellular acidity, a “reappreciated” trait of tumor environment driving malignancy: perspectives in diagnosis and therapy. *Cancer Metastasis Rev*. 2014;33:823–832. doi:10.1007/s10555-014-9506-4
13. Boedtkjer E, Pedersen SF. The acidic tumor microenvironment as a driver of cancer. *Annu Rev Physiol*. 2020;82:103–126. doi:10.1146/annurev-physiol-021119-034627
14. Rohani N, Hao L, Alexis MS, et al. Acidification of tumor at stromal boundaries drives transcriptome alterations associated with aggressive phenotypes. *Cancer Res*. 2019;79:1952–1966. doi:10.1158/0008-5472.CAN-18-1604
15. Tufail M, Jiang CH, Li N. Altered metabolism in cancer: insights into energy pathways and therapeutic targets. *Mol Cancer*. 2024;23:203. doi:10.1186/s12943-024-02119-3
16. Mao Y, Zhang J, Zhou Q, et al. Hypoxia induces mitochondrial protein lactylation to limit oxidative phosphorylation. *Cell Res*. 2024;34:13–30. doi:10.1038/s41422-023-00864-6
17. Zhu F, Crombie JL, Ni W, et al. Hypomethylating agent decitabine sensitizes diffuse large B-cell lymphoma to venetoclax. *Haematologica*. 2024;109:186–199. doi:10.3324/haematol.2023.283245
18. Akbari M, Kirkwood TBL, Bohr VA. Mitochondria in the signaling pathways that control longevity and health span. *Ageing Res Rev*. 2019;54:100940. doi:10.1016/j.arr.2019.100940
19. Deng Y, Su W, Zhu J, et al. Helicobacter pylori infection disturbs the tumor immune microenvironment and is associated with a discrepant prognosis in gastric de novo diffuse large B-cell lymphoma. *J Immunother Cancer*. 2021;9.
20. Garnock-Jones KP. Vonoprazan: first global approval. *Drugs*. 2015;75:439–443. doi:10.1007/s40265-015-0368-z
21. Zhuang Q, Chen S, Zhou X, et al. Comparative efficacy of P-CAB vs proton pump inhibitors for grade C/D esophagitis: a systematic review and network meta-analysis. *Am J Gastroenterol*. 2024;119:803–813. doi:10.14309/ajg.0000000000002714
22. Lu X, Song Z, Hao J, et al. Proton pump inhibitors enhance macropinocytosis-mediated extracellular vesicle endocytosis by inducing membrane v-ATPase assembly. *J Extracell Vesicles*. 2024;13:e12426.
23. Yu J, Lv YM, Yang P, et al. Safety and effectiveness of vonoprazan-based rescue therapy for Helicobacter pylori infection. *World J Gastroenterol*. 2023;29:3133–3144. doi:10.3748/wjg.v29.i20.3133
24. Sugano K. Vonoprazan fumarate, a novel potassium-competitive acid blocker, in the management of gastroesophageal reflux disease: safety and clinical evidence to date. *Therap Adv Gastroenterol*. 2018;11:1756283X17745776. doi:10.1177/1756283X17745776
25. Scott DR, Munson KB, Marcus EA, et al. The binding selectivity of vonoprazan (TAK-438) to the gastric H+, K+ -ATPase. *Aliment Pharmacol Ther*. 2015;42:1315–1326. doi:10.1111/apt.13414
26. Sa K, Almatroudi A, Alsahli MA, et al. novel strategies for disrupting cancer-cell functions with mitochondria-targeted antitumor drug-loaded nanoformulations. *Int J Nanomed*. 2021;16:3907–3936. doi:10.2147/IJN.S303832
27. Jiang K, Tian K, Yu Y, et al. Kupffer cells determine intrahepatic traffic of PEGylated liposomal doxorubicin. *Nat Commun*. 2024;15:6136. doi:10.1038/s41467-024-50568-7
28. Manfroi B, De Grandis M, Moreaux J, et al. The microenvironment of DLBCL is characterized by noncanonical macrophages recruited by tumor-derived CCL5. *Blood Adv*. 2021;5:4338–4351. doi:10.1182/bloodadvances.2021004203
29. Liu M, Bertolazzi G, Sridhar S, et al. Spatially-resolved transcriptomics reveal macrophage heterogeneity and prognostic significance in diffuse large B-cell lymphoma. *Nat Commun*. 2024;15:2113. doi:10.1038/s41467-024-46220-z
30. Gao C, Huang Q, Liu C, et al. Treatment of atherosclerosis by macrophage-biomimetic nanoparticles via targeted pharmacotherapy and sequestration of proinflammatory cytokines. *Nat Commun*. 2020;11:2622. doi:10.1038/s41467-020-16439-7
31. Cao Z, Liu X, Zhang W, et al. Biomimetic macrophage membrane-camouflaged nanoparticles induce ferroptosis by promoting mitochondrial damage in Glioblastoma. *ACS Nano*. 2023;17:23746–23760. doi:10.1021/acsnano.3c07555
32. Han R, Ren Z, Wang Q, et al. Synthetic biomimetic liposomes harness efferocytosis machinery for highly efficient macrophages-targeted drug delivery to alleviate inflammation. *Adv Sci*. 2024;11:e2308325.
33. Anghelache M, Voicu G, Deleanu M, et al. Biomimetic nanocarriers of pro-resolving lipid mediators for resolution of inflammation in atherosclerosis. *Adv Healthc Mater*. 2024;13:e2302238.
34. Zhang Y, Li TT, Wang Z, et al. Coaxial microfluidic spinning design produced high strength alginate membranes for antibacterial activity and drug release. *Int J Biol Macromol*. 2023;243:124956. doi:10.1016/j.ijbiomac.2023.124956
35. Zhang J, Zhang Q. Using seahorse machine to measure OCR and ECAR in cancer cells. *Methods Mol Biol*. 2019;1928:353–363.

36. Li Y, Ran Q, Duan Q, et al. 7-Dehydrocholesterol dictates ferroptosis sensitivity. *Nature*. 2024;626:411–418. doi:10.1038/s41586-023-06983-9
37. Echizen H. The first-in-class potassium-competitive acid blocker, Vonoprazan Fumarate: pharmacokinetic and pharmacodynamic considerations. *Clin Pharmacokinet*. 2016;55:409–418. doi:10.1007/s40262-015-0326-7
38. Zheng C, Zhang D, Kong Y, et al. Dynamic regulation of drug biodistribution by turning tumors into decoys for biomimetic nanoplatform to enhance the chemotherapeutic efficacy of breast cancer with bone metastasis. *Exploration*. 2023;3:20220124. doi:10.1002/EXP.20220124
39. Wu H, Liu Y, Liu Q, et al. HMMR triggers immune evasion of hepatocellular carcinoma by inactivation of phagocyte killing. *Sci Adv*. 2024;10:eadl6083.
40. Lu M, Xing H, Shao W, et al. Antitumor synergism between PAK4 silencing and immunogenic phototherapy of engineered extracellular vesicles. *Acta Pharm Sin B*. 2023;13:3945–3955. doi:10.1016/j.apsb.2023.03.020
41. Desousa BR, Kim KK, Jones AE, et al. Calculation of ATP production rates using the Seahorse XF Analyzer. *EMBO Rep*. 2023;24:e56380.
42. Wang H, Ye J, Peng Y, et al. CKLF induces microglial activation via triggering defective mitophagy and mitochondrial dysfunction. *Autophagy*. 2024;20:590–613. doi:10.1080/15548627.2023.2276639
43. Przystal JM, Cianciolo Cosentino C, Yadavilli S, et al. Imipridones affect tumor bioenergetics and promote cell lineage differentiation in diffuse midline gliomas. *Neuro Oncol*. 2022;24:1438–1451. doi:10.1093/neuonc/noac041
44. Hoang NM, Liu Y, Bates PD, et al. Targeting DNMT3A-mediated oxidative phosphorylation to overcome ibrutinib resistance in mantle cell lymphoma. *Cell Rep Med*. 2024;5:101484. doi:10.1016/j.xcrm.2024.101484
45. Jana S, Shang J, Hong JY, et al. A Mitochondria-targeting SIRT3 inhibitor with activity against diffuse large B Cell Lymphoma. *J Med Chem*. 2024;67:15428–15437. doi:10.1021/acs.jmedchem.4c01053
46. Wang X, Liu H, Fei Y, et al. Metabolic pathway-based subtyping reveals distinct microenvironmental states associated with diffuse large B-cell lymphoma outcomes. *Hematol Oncol*. 2024;42:e3279.
47. Jean SR, Ahmed M, Lei EK, et al. Peptide-mediated delivery of chemical probes and therapeutics to Mitochondria. *Acc Chem Res*. 2016;49:1893–1902. doi:10.1021/acs.accounts.6b00277
48. Qian K, Gao S, Jiang Z, et al. Recent advances in mitochondria-targeting theranostic agents. *Exploration*. 2024;4:20230063. doi:10.1002/EXP.20230063
49. Selvaraj S, Chauhan A, Dutta V, et al. A state-of-the-art review on plant-derived cellulose-based green hydrogels and their multifunctional role in advanced biomedical applications. *Int J Biol Macromol*. 2024;265:130991. doi:10.1016/j.ijbiomac.2024.130991
50. Selvaraj S, Chauhan A, Verma R, et al. Role of degrading hydrogels in hepatocellular carcinoma drug delivery applications: a review. *J Drug Delivery Sci Technol*. 2024;95:105628. doi:10.1016/j.jddst.2024.105628
51. Corazzelli G, Frigeri F, Arcamone M, et al. Biweekly rituximab, cyclophosphamide, vincristine, non-pegylated liposome-encapsulated doxorubicin and prednisone (R-COMP-14) in elderly patients with poor-risk diffuse large B-cell lymphoma and moderate to high 'life threat' impact cardiopathy. *Br J Haematol*. 2011;154:579–589. doi:10.1111/j.1365-2141.2011.08786.x
52. Tang W, Yang Y, Yang L, et al. Macrophage membrane-mediated targeted drug delivery for treatment of spinal cord injury regardless of the macrophage polarization states. *Asian J Pharm Sci*. 2021;16:459–470. doi:10.1016/j.ajps.2021.03.005
53. Zhang Y, Cai K, Li C, et al. Macrophage-membrane-coated nanoparticles for tumor-targeted chemotherapy. *Nano Lett*. 2018;18:1908–1915. doi:10.1021/acs.nanolett.7b05263
54. Xiao T, He M, Xu F, et al. Macrophage membrane-camouflaged responsive polymer nanogels enable magnetic resonance imaging-guided chemotherapy/chemodynamic therapy of orthotopic Glioma. *ACS Nano*. 2021;15:20377–20390. doi:10.1021/acsnano.1c08689
55. Gong J, Shi T, Liu J, et al. Dual-drug codelivery nanosystems: an emerging approach for overcoming cancer multidrug resistance. *Biomed Pharmacother*. 2023;161:114505. doi:10.1016/j.biopha.2023.114505